

A STABLE CARDINALITY DISTANCE FOR TOPOLOGICAL CLASSIFICATION

VASILEIOS MAROULAS, CASSIE PUTMAN MICUCCI, AND ADAM SPANNAUS

ABSTRACT. This work incorporates topological and geometric features via persistence diagrams to classify point cloud data arising from materials science. Persistence diagrams are planar sets that summarize the shape details of given data. A new metric on persistence diagrams generates input features for the classification algorithm. The metric accounts for the similarity of persistence diagrams using a linear combination of matching costs and cardinality differences. Investigation of the stability properties of this metric provides theoretical justification for the use of the metric for comparisons of such diagrams. The crystal structure of materials are successfully classified based on noisy and sparse data retrieved from synthetic Atomic Probe Tomography experiments.

1. INTRODUCTION

A crucial first step in understanding properties of a material is determining its crystal structure. For highly disordered metallic alloys, such as High Entropy Alloys (HEAs), Atomic Probe Tomography (APT) gives a snapshot of the local atomic environment. APT has two main drawbacks: experimental noise and missing data. Approximately 67% of the atoms in a sample are not registered in a typical experiment, and those atoms that are captured have their spatial coordinates corrupted by experimental noise. This work provides a machine learning approach to classifying the crystal structure of high entropy alloys based on the mean and variance of the distances when compared with related and dissimilar crystal structures. The goal is to classify the true crystal lattice of a noisy and sparse materials dataset, where the unit cells are either Body centered cubic (BCC) or Face centered cubic (FCC). The BCC structure has a single atom in the center of the cube, while the FCC has a void in its center but has atoms on the center of the cubes' faces.

A related approach to classifying crystal structures of defective materials using deep learning was proposed by [1]. The authors employ a convolutional neural network for classifying the crystal structure by looking at a diffraction image. Furthermore, the authors suggest their method could be used to determine the crystal structure of APT data or other defective materials data. However, the synthetic data considered in [1] is not a realistic representation of experimental APT data, where about 67% of the data is missing [2, 3, 4] and is corrupted by more observational noise [3] than considered by [1].

Homology is applicable to this problem as it is a branch of topology that studies and differentiates shapes [5]. It provides a summary of the connectedness and structure of an object. The distinction between BCC and FCC point clouds is captured well by the homology and explains the high degree of accuracy in the classification scheme presented herein. Topological Data Analysis (TDA) uncovers topological and homological features

Key words and phrases. Classification, Atomic Probe Tomography, Persistence Diagram Metric, Cardinality, Homology, Machine Learning .

This work has been partially supported by the ARO Grant # W911NF-17-1-0313, and the NSF DMS-1821241.

of the data and provides a summary for machine learning algorithms, as well as a useful toolbox for classification. Several authors have investigated the persistent homology of point clouds generated from data and developed a framework to use TDA on such problems [6, 7, 8, 9, 10, 11, 12, 13]. Persistent homology records when different homological features emerge and vanish in the data. This topological analysis quantifies the significance of a homological feature and provides a tool to contend with noisy data. The birth and death of each homological feature is calculated and recorded in a persistence diagram. Persistence diagrams yield a topological summary of the persistent homology of a dataset and are rich sources of detail about underlying geometric features. The diagrams could be used in distance-based classifiers or vectorized and input into standard classification algorithms, such as support vector machines [14].

Using a metric-based approach provides a way to compare persistence diagrams. The Wasserstein and bottleneck distances compute the cost of an optimal matching between the points in each persistence diagram, while allowing matching to additional points on the diagonal to allow for cardinality differences and to prove stability properties [15]. Motivated by [16] we consider here the d_p^c metric. This metric leverages the cardinality of the persistence diagrams, as well as distances between points in the diagrams. It calculates the cost of matching the points of the diagram with smaller cardinality to points in the diagram with larger cardinality. Points that are leftover from differences in cardinality are penalized by a pertinent parameter.

The stability properties of the metric are shown in this paper. Specifically, stability guarantees that when the distances between point clouds go to zero, the distances between the associated persistence diagrams vanish to zero as well. Another notion of stability is given in [17]; using a related approach, we show continuity of the mapping of point cloud to persistence diagram under the d_p^c metric. The analysis provides insight into how the cardinality of the diagrams changes with the cardinality of the input point clouds. Additionally, using statistics on the cardinality generates corresponding prediction intervals, which give probabilistic bounds on the distances between the persistence diagrams. The idea is that point clouds generated from the same process have small variability with respect to cardinality of the persistence diagrams. This reasoning proves useful in data analysis.

The work is organized as follows. Relevant definitions and concepts necessary for persistent homology are presented in Section 2. Stability results of the d_p^c metric are in Section 3, as well as confidence interval bounds. Section 4 demonstrates a classification scheme for materials science data retrieved from synthetic APT experiments. We conclude in Section 5.

2. PERSISTENT HOMOLOGY BACKGROUND

This section explains the construction of persistence diagrams, which are topological summaries of the underlying space. The Vietoris-Rips complex provides the necessary computational link between the point cloud and its persistence diagram. To compute the Vietoris-Rips complex, a strictly increasing sequence $\{\epsilon_i\}$ is created. Then one calculates the homology of $\cup_q B(q; \epsilon_i)$, the union of balls of radius ϵ_i centered at each point q in the point cloud. Then at each ϵ_i the homology of the Vietoris-Rips complex is computed. For an illustration, see Figs. 1A to 1D. Instead of analyzing the Vietoris-Rips complex at different values of ϵ_i , denoted by VR_{ϵ_i} , it is clear that $VR_{\epsilon_j} \subset VR_{\epsilon_k}$ for $j < k$ since the sequence $\{\epsilon_i\}$ is increasing by construction. Thus we may examine specific ϵ values corresponding to the emergence and disappearance of homological features.

As can be seen in Fig. 1, a 0-dim homological feature is a connected component of a simplex, and a dimension 1 feature is a 1-dim hole, such as the inside of a circle. Similarly, 2-dim homology describes voids, such as the inside of a sphere. Higher dimensions yield analogous holes. These features describe and differentiate point clouds, proving themselves useful in classification problems. The k -dim homology ($k = 0, 1, 2, \dots$) of a topological space is also summarized by its associated k th Betti number, β_k , which gives the number of k -dim features present. For example, β_0 is the number of connected components. (For point clouds, β_0 is also the size of the point cloud and the cardinality of the 0-dim persistence diagram.) β_1 is the number of 1-dim holes (such as the inside of a circle). We provide formal definitions [18]:

Definition 2.1. An abstract simplicial complex σ is a collection of simplices such that for every set A in σ and every nonempty set $B \subset A$, we have that B is in σ .

Definition 2.2. The Vietoris-Rips complex is a simplicial complex formed from a set such that corresponding to each subset of n points of the set, an n -simplex is included in the Vietoris-Rips complex each time the subsets have pairwise distances at most some threshold ϵ .

This homological summary of the data is plotted as an ordered pair (b, d) in a persistence diagram, where b denotes the birth of a feature and d its death. Persistence diagrams can also be computed using a function g from a topological space to \mathbb{R} . Homological features are born and die within the sublevel sets $g^{-1}(-\infty, t]$ as t increases. Such a function can act as an approximation to a point cloud; typical functions used are kernel density estimators [19] and the distance to measure [20]. These birth and death times create another persistence diagram, see Fig. 1F.

To calculate the similarity between diagrams for classification problems, a metric on the space of persistence diagrams is needed, e.g. the Wasserstein distance. The Wasserstein distance for persistence diagrams can be thought of as a matching problem with associated costs for each pairing of points, as explained in [21].

Definition 2.3. The p -Wasserstein distance between two persistence diagrams X and Y is given by $W_p(X, Y) = \left(\inf_{\eta: X \rightarrow Y} \sum_{x \in X} \|x - \eta(x)\|_\infty^p \right)^{\frac{1}{p}}$, where the infimum is taken over all such bijections, and the points of the diagonal are added with infinite multiplicity to each diagram.

In the Wasserstein distance, points in one diagram are matched to the points of the other diagram (including points on the diagonal with each diagonal point having infinite multiplicity), see Fig. 2A. The cost of each matching is the infinity norm between the two points, if the two points are not both on the diagonal. Diagonal points can be matched to each other for free, i.e. with no cost for matching the points.

The bottleneck distance is the limit of the Wasserstein distance as $p \rightarrow \infty$, and as such, the bottleneck distance only looks at the worst matching of the bijection. Allowing points to be matched to the diagonal in these distances ensures stability and the existence of a bijection between the two diagrams, since the two diagrams may have different cardinalities. However, the cardinality can be a more or less important feature of the diagram, and the Wasserstein and bottleneck distances may not catch distinctions in cardinality between diagrams.

To that end, the d_p^c metric [16] takes into account the cardinality of the diagrams. The d_p^c distance allows one to decide how important the cardinality difference is for calculating the distance. A smaller c accounts for local geometric differences, while a larger c focuses

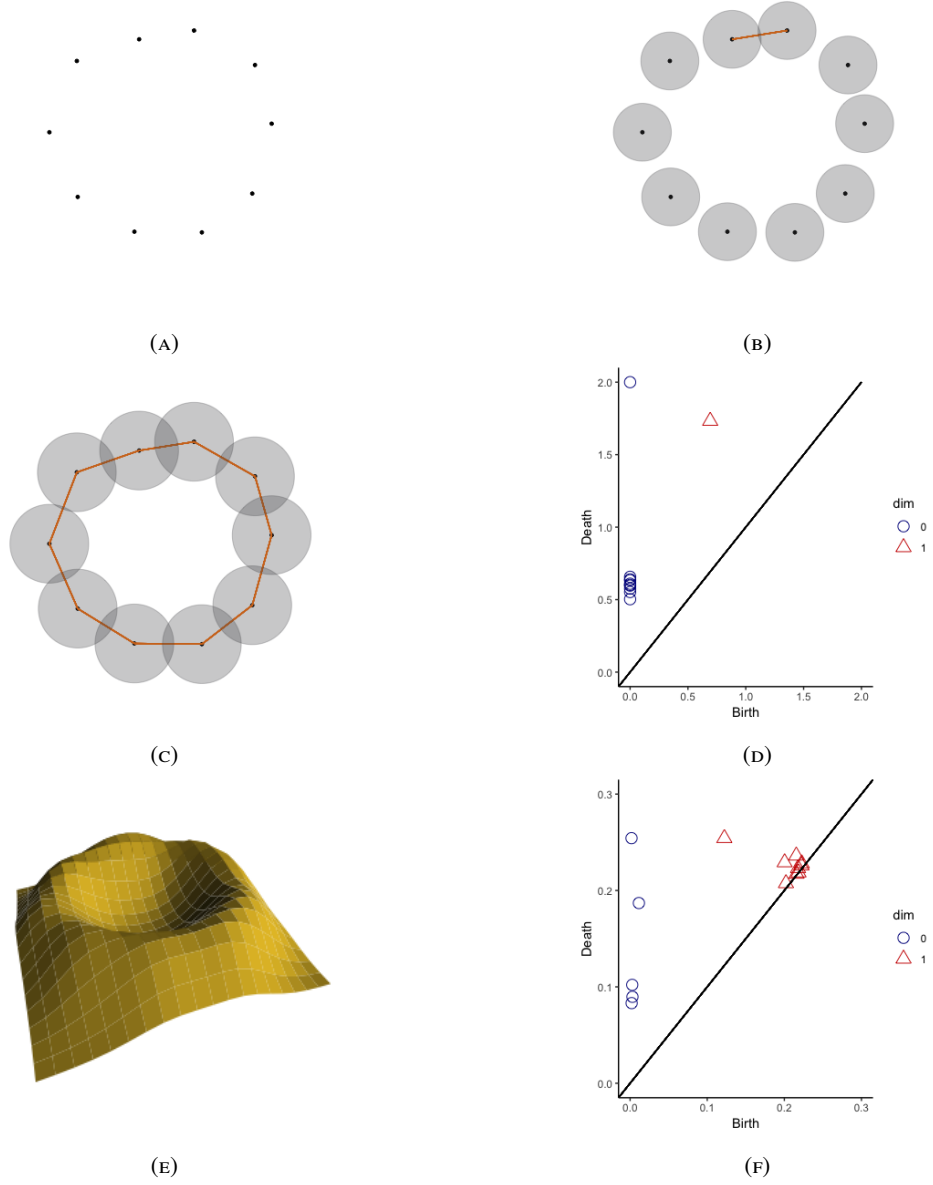


FIGURE 1. Begin with a point cloud (A). After increasing the radius of the balls around the points a 1-simplex (line segment) forms, (B). Eventually, more 1-simplices are added and a 1-dim hole forms (C). In (D), the persistence diagram tracks all the birth and death times with respect to the radius ϵ of the homological features for each dimension. Using the same points as in (A), the kernel density estimator function is plotted in (E). A corresponding persistence diagram is created using sublevel sets in (F).

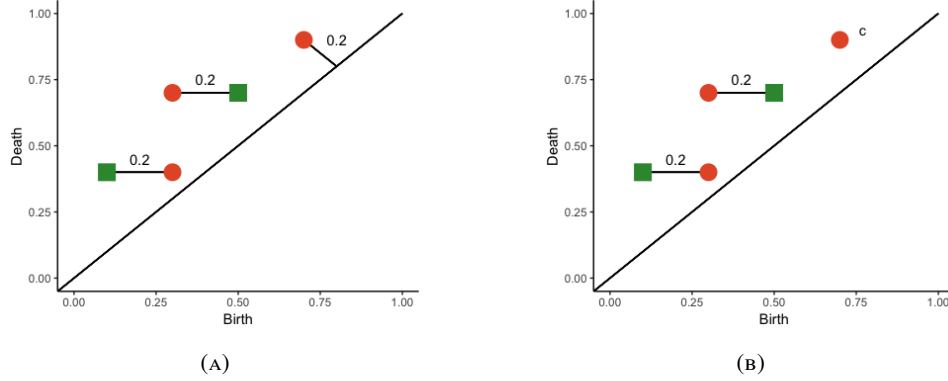


FIGURE 2. Consider two persistence diagrams, one given by the green squares and another by the orange circles. The Wasserstein distance (A) imposes a cost of 0.2 to the extra orange point (the L_∞ distance to the diagonal). The d_p^c distance (B) imposes a penalty c on the point instead.

on the global geometric and topological scale. It is precisely by considering differences in cardinality that the d_p^c metric can distinguish between geometric features of the point cloud that other metrics may miss.

Definition 2.4. Let X and Y be two persistence diagrams with cardinalities n and m respectively such that $n \leq m$. Let $X = \{x_1, \dots, x_n\}$ and $Y = \{y_1, \dots, y_m\}$. Let $c > 0$ and $1 \leq p < \infty$ be fixed parameters. The d_p^c distance between two persistence diagrams X and Y is

$$(1) \quad d_p^c(X, Y) = \left(\frac{1}{m} \left(\min_{\pi \in \Pi_m} \sum_{i=1}^n \min(c, \|x_i - y_{\pi(i)}\|_\infty)^p + c^p |m - n| \right) \right)^{\frac{1}{p}},$$

where Π_m is the set of permutations of $(1, \dots, m)$. If $|X| := \text{card}(X) > |Y|$, define $d_p^c(X, Y) := d_p^c(Y, X)$.

3. STABILITY PROPERTIES FOR d_p^c DISTANCE

The stability of the d_p^c distance is proved in this section. Stability of the distances means that small perturbations in the underlying space result in small perturbations of the persistence diagrams. Here the perturbations are measured by the d_p^c distance. Adopting the approach of estimating a point cloud via a pertinent function, e.g. a kernel density estimator [19], persistence diagrams may be constructed using sublevel sets as in Fig. 1F. Their differences can be computed using the Wasserstein and bottleneck distances. Using this functional representation, stability of the Wasserstein and bottleneck distances has been shown in [15] and [18], respectively. Considering point clouds whose distances shrink to zero, Theorem 3.1 shows that the distance between persistence diagrams goes to zero as well.

Theorem 3.1 (Stability Theorem). *Let $c \in (0, \infty)$ and $p \in \mathbb{N}$ be given. Let A be a finite nonempty point cloud in \mathbb{R}^n . Suppose that $\{A_i\}_{i \in \mathbb{N}}$ is a sequence of finite nonempty point clouds such that $d_p^c(A, A_i) \rightarrow 0$ as $i \rightarrow \infty$. Let X^δ and X_i^δ be the δ -dim persistence diagrams*

created from the Vietoris-Rips complex for A and A_i respectively. Then $d_p^c(X^\delta, X_i^\delta) \rightarrow 0$ as $i \rightarrow \infty$.

Note that Theorem 3.1 does not depend on a function created from the points, but simply on the points themselves and the Vietoris-Rips complex generated from the points. Another way of stating Theorem 3.1 is that $\lim_{n \rightarrow \infty} A_i = A$ in the space of point clouds under the d_p^c metric implies that $\lim_{n \rightarrow \infty} X_i^\delta = X^\delta$ in the space of persistence diagrams endowed with the d_p^c metric, i.e. the mapping from a point cloud to the persistence diagram of its Vietoris-Rips complex is continuous under the d_p^c metric. Lemma 3.2 shows that if the d_p^c distance between the underlying point clouds goes to 0, then eventually the cardinality of the point clouds must be the same.

Lemma 3.2. *If $d_p^c(A, A_i) \rightarrow 0$ as $i \rightarrow \infty$, then $|A_i| = |A|$ for $i \geq N_0$ for some $N_0 \in \mathbb{N}$.*

Proof. Suppose that $|A_i| \neq |A|$ infinitely often. Since $d_p^c(A, A_i) \rightarrow 0$, for every $\epsilon > 0$, there is an $N \in \mathbb{N}$ such that $i \geq N$ implies that $d_p^c(A, A_i) < \epsilon$. Let $\epsilon = \frac{c}{|A|+1}$, noting that $|A|$ is fixed. By assumption $|A_i| < |A|$, $|A_i| > |A|$, or both, infinitely often. If $|A| < |A_i|$, then by Def. 2.4

$$(2) \quad d_p^c(A, A_i) \geq \left(c^p \frac{|A_i| - |A|}{|A_i|} \right)^{\frac{1}{p}} \geq c \frac{|A_i| - |A|}{|A_i|}.$$

The function $h : \mathbb{N} \rightarrow \mathbb{R}$ given by $h(z) = \frac{z-|A|}{z}$ is strictly increasing. Whenever $|A| < |A_i|$, we have $|A_i| \geq |A| + 1$. The restriction of h to $\{|A| + 1, |A| + 2, |A| + 3, \dots\}$ achieves its minimum at $|A| + 1$. This shows that the RHS of Eq. (2) is greater than or equal to $\frac{c}{|A|+1}$, whenever $|A| < |A_i|$, which by assumption happens infinitely often. This contradicts $d_p^c(A, A_i) < \epsilon$ for all $i \geq N$. The case where $|A| > |A_i|$ follows similarly. \square

Lemma 3.3. *Suppose the points of each point cloud A_i are ordered so that $A_i = \{a_{\pi_i(1)}, a_{\pi_i(2)}, \dots, a_{\pi_i(|A|)}\}$. Let D_A and D_{A_i} be the distance matrices for the points of A and A_i respectively, i.e., the kl -th entry of D_A is $\|a_k - a_l\|_n$. Then,*

- (i) $\|D_A - D_{A_i}\|_\infty \rightarrow 0$ as $i \rightarrow \infty$, and
- (ii) for some $N_1 \in \mathbb{N}$, the order of the entries of the upper triangular portion of D_A and D_{A_i} is the same for $i \geq N_1$, up to permutation when either D_A or D_{A_i} have duplicate entries.

Proof. (i) Let $A = \{a_1, \dots, a_k\}$, $A_i = \{a_1^i, \dots, a_k^i\}$, and $\lambda_\alpha^i = \|a_\alpha - a_{\pi_i(\alpha)}^i\|_n$ for the bijection π_i in the d_p^c distance between A_i and A . Suppose that $d_p^c(A, A_i) \rightarrow 0$. Note that since c is fixed, there is some N_c such that eventually $d_p^c(A_i, A) = \left(\frac{1}{|A|} \min_{\pi_i \in \Pi_{|A|}} \sum_{\ell=1}^{|A|} \|a_\ell - a_{\pi_i(\ell)}^i\|_n^p \right)^{\frac{1}{p}}$ for $i \geq N_c$. $d_p^c(A, A_i) \rightarrow 0$, which shows that $|A|^{-\frac{1}{p}} \|\lambda\|_p \rightarrow 0$ as $i \rightarrow \infty$. Thus $\|\lambda^i\|_p \rightarrow 0$ as $i \rightarrow \infty$.

Now, let $E = D_A - D_{A_i}$.

$$\begin{aligned} \|E_{kl}\|_\infty &= \max_{k,l} \left| \|a_k - a_l\|_n - \|a_k^i - a_l^i\|_n \right| \\ &= \max_{k,l} \left| \|a_k - a_l\|_n + \|a_l - a_k^i\|_n - \|a_l - a_k^i\|_n - \|a_k^i - a_l^i\|_n \right| \\ &\leq \left| \|a_k - a_l\|_n - \|a_l - a_k^i\|_n \right| + \left| \|a_k^i - a_l^i\|_n - \|a_l - a_k^i\|_n \right| \\ (3) \quad &\leq \|a_k - a_k^i\|_n + \|a_l - a_l^i\|_n \end{aligned}$$

Eq. (3) goes to 0 as $i \rightarrow \infty$, proving (i).

(ii) Suppose that the m distinct upper triangular entries of D_A are ordered from smallest

to largest, say $d_1^A < d_2^A < \dots < d_m^A$, where $m \leq |A|(|A| - 1)/2$. For $\eta \in \{1, \dots, m+1\}$ let $h_\eta \subset [0, \infty)$ be a sequence such that $h_1 < d_1^A < h_2 < d_2^A < \dots < h_m < d_m^A < h_{m+1}$. Let $\|D_A - D_{A_i}\|_\infty < \frac{h}{2}$, where $h = \min_{\eta_1, \eta_2 \in \{1, \dots, m+1\}} \{|h_{\eta_1} - h_{\eta_2}|\}$. We show that there exists a sequence g_η such that $|h_\eta - g_\eta| < 2h$ for each $\eta \in \{1, \dots, m+1\}$ and $h_\eta < d_j^A < h_{\eta+1}$ implies $g_\eta < d_j^{A_i} \leq g_{\eta+1}$. Let $h_\eta < d_j^A < h_{\eta+1}$, and suppose that it is not the case that $h_\eta < d_j^{A_i} \leq h_{\eta+1}$. Since $\|D_A - D_{A_i}\|_\infty < \frac{h}{2}$, then either $d_j^{A_i} \in (h_{\eta-1}, h_\eta]$ or $d_j^{A_i} \in (h_{\eta+1}, h_{\eta+2}]$. If the first case is true, then take $g_\eta = d_j^A - \frac{h}{2}$. If the second, then take $g_\eta = d_j^A + \frac{h}{2}$. This proves the existence of the sequence. Now proceeding by contradiction, if the lemma does not hold for some entries $d_j^A \in D_A$ and $d_j^{A_i} \in D_{A_i}$, then take $\|D_A - D_{A_i}\|_\infty < \frac{1}{2}|d_j^A - d_j^{A_i}|$. \square

Proof (Theorem 3.1). By Lemma 3.2, take $|A_i| = |A|$ without loss of generality. By Lemma 3.3 (i), $\|D_A - D_{A_i}\|_\infty \rightarrow 0$ as $i \rightarrow \infty$. If the Vietoris-Rips complex were computed at every threshold value in $[0, \infty)$, then the birth and death times of all features of all dimensions would be distances between points in the underlying point cloud (including the birth time of 0 in the 0-dim diagram). Since the order of the entries of D_A and D_{A_i} may be taken to be the same from Lemma 3.3 (ii), the same number of simplices are formed in the complexes for A and A_i for each dimension of simplex. Also, the labels of the simplices according to the points of A and A_i are given from the bijection π_i in Lemma 3.3 (i).

Now, for 0-dim it is clear that for the cardinalities of the persistence diagrams $|X^0| = |X_i^0|$ since for the cardinalities of their associated point clouds, $|A_i| = |A|$. For a higher dimensional feature ($\delta \geq 1$) to appear in the complex, we must have that a certain number of the distances are less than or equal to the threshold ϵ and a certain number of the distances are greater than ϵ . Lemma 3.3 (ii) shows that although the thresholds where the features are created may be different, the same number of features are formed in the Vietoris-Rips complexes of A and A_i , and these features are formed in the same order and with the points that correspond under π_i .

If $X^\delta = \{x_1, x_2, \dots, x_{|X^\delta|}\}$ and $X_i^\delta = \{x_1, x_2, \dots, x_{|X_i^\delta|}\}$, then we have that $|X^\delta| = |X_i^\delta|$ and that $d_p^c(X^\delta, X_i^\delta) < 2h$. Thus $d_p^c(X^\delta, X_i^\delta) \rightarrow 0$ as $i \rightarrow \infty$.

To provide a practical way to control c and consequently compute the possible fluctuations of d_p^c distance, a probabilistic upper bound is provided relying on least squares. Specifically, the following analysis gives predictions on the number of 1-dim features present in the persistence diagram, which we denote b_1 , based on the size of the point cloud $|A|$. Similarly, denote by b_0 the number of 0-dim features in the persistence diagram. Note that $b_0 = \beta_0$ for the point cloud, but $b_1 \neq \beta_1$.

Proposition 3.4. For n , the cardinality of a point cloud, the possible range of b_1 contains $[0, \lfloor \frac{n}{2} \rfloor - 1] \cap \mathbb{N}$.

Proof. To form a point cloud with n points that has $b_1 = 0$, simply take the n points and arrange them on a line. To form a point cloud with n points that has $b_1 = \lfloor \frac{n}{2} \rfloor - 1$, arrange the n points in two rows each with $\lfloor \frac{n}{2} \rfloor$ points. Set the spacing between adjacent points in each of the rows to be 1 and then place the two rows directly beside each other so that for each point in the first row, there is exactly one point in the second row at a distance of 1. Adding lines appropriately creates $b_1 = \lfloor \frac{n}{2} \rfloor - 1$ squares with side length 1. Thus, creating the Vietoris-Rips complex and corresponding diagram gives exactly $b_1 = \lfloor \frac{n}{2} \rfloor - 1$ for the 1-dim persistence diagram. For an illustration of the arrangement, see Fig. 3. \square



FIGURE 3. An example of the configuration of points in the proof of Proposition 3.4 for 12 points.

Let n point clouds be generated from some process, and n corresponding persistence diagrams be created. For each persistence diagram $X_i^\delta, \delta \in \{0, 1\}$, record the cardinality of the 0-dim diagram in $\mathbf{b}_0 = (b_0^1, \dots, b_0^n)$ and of the 1-dim diagram in $\mathbf{b}_1 = (b_1^1, \dots, b_1^n)$. Proposition 3.4 suggests a relationship between b_0 and b_1 summarized below:

$$(4) \quad \mathbf{b}_1 = \psi(\mathbf{b}_0) + \boldsymbol{\epsilon},$$

where $\boldsymbol{\epsilon} \sim \mathcal{N}(0, \sigma^2)$ captures perturbations from the mean pattern and $\mathbf{b}_0 \in \mathbb{R}^{n \times 2}$ is the predictor matrix whose rows are $(b_0^i \ 1)$. Proposition 3.4, however, gives that the possible range of \mathbf{b}_1 is increasing as \mathbf{b}_0 grows, which yields that an increase in variance as \mathbf{b}_0 grows may be present. Thus the analysis of the change in number of 1-dim features as the size of the point cloud changes needs to account for heteroscedasticity. Therefore to estimate the number of 1-dim holes by Eq. (4), we use weighted least squares [23]. If $\mathbf{W} \in \mathbb{R}^{n \times n}$ is the weight matrix $\mathbf{W} = \text{diag}(a_1, \dots, a_n)$, then a weighted least-squares regression can be found for $\mathbf{b}_1 = \mathbf{b}_0 \boldsymbol{\gamma} + \boldsymbol{\epsilon}$, where $\epsilon_i \sim \mathcal{N}(0, \sigma_i^2)$. The approximation is then given by $\mathbf{b}_0 \hat{\boldsymbol{\gamma}} = \mathbf{b}_1$, with $\hat{\boldsymbol{\gamma}} = (\mathbf{b}_0^T \mathbf{W} \mathbf{b}_0)^{-1} \mathbf{b}_0^T \mathbf{W} \mathbf{b}_1$. In turn, Proposition 3.5 gives prediction intervals using weighted least squares for the d_p^c distance. Note that the same analysis could be used for a transformation of the predictor \mathbf{b}_0 , as we see later in Fig. 8.

Proposition 3.5. Assume the model $\mathbf{b}_1 = \mathbf{b}_0 \boldsymbol{\gamma} + \boldsymbol{\epsilon}$, where $\epsilon_i \sim \mathcal{N}(0, \sigma_i)$ depends on the value of the input b_0^i . Let X^1 and Y^1 be persistence diagrams generated from the same process as \mathbf{b}_0 with $|X^0| = n$. Considering the $(1 - \alpha) \cdot 100\%$ -level confidence bound for the cardinalities \mathbf{b}_0 and \mathbf{b}_1 , the distance $d_p^c(X^1, Y^1)$ is bounded by

$$\left(\min_{\pi \in \Pi_m} \sum_{i=1}^n \min(c, \|x_i^1 - y_{\pi(i)}^1\|_\infty)^p + c^p 2t_{1-\alpha, n-2} s \sqrt{(1/n)(\mathbf{b}_0^T \mathbf{W} \mathbf{b}_0)^{-1}(1/n)^T + n} \right)^{\frac{1}{p}}.$$

Proof. Prediction intervals can be constructed for the cardinality of the 1-dim diagram for point cloud size b_0^* using standard results on weighted least squares. Specifically, for level $(1 - \alpha) \cdot 100\%$ a confidence interval for the new response \hat{b}_1^* is sought. To calculate this interval for a new response from the mean predicted response $\hat{b}_1^* = \hat{\boldsymbol{\gamma}} b_0^*$, note that $\hat{b}_1^* - b_1^*$ has the distribution $\frac{\hat{b}_1^* - b_1^*}{\text{Var}(\hat{b}_1^* - b_1^*)} \sim t_{n-2}$. Also, $\text{Var}(\hat{b}_1^* - b_1^*) = \text{Var}(\boldsymbol{\epsilon})(1/b_0^*)(\mathbf{b}_0^T \mathbf{W} \mathbf{b}_0)^{-1}(1/b_0^*)^T + \frac{\text{Var}(\boldsymbol{\epsilon})}{w^*}$, where $w^* = \frac{1}{b_0^*}$, the weight corresponding to b_0^* . Prediction intervals for b_1^* are thus $\hat{b}_1^* \pm t_{1-\alpha/2, n-2} s \sqrt{(1/b_0^*)(\mathbf{b}_0^T \mathbf{b}_0)^{-1}(1/b_0^*)^T + b_0^*}$, where $s^2 = \frac{\hat{\boldsymbol{\epsilon}}^T \mathbf{W} \hat{\boldsymbol{\epsilon}}}{n-2}$, the unbiased estimator for $\text{Var}(\boldsymbol{\epsilon})$, using the residuals $\hat{\boldsymbol{\epsilon}}$. \square

4. CLASSIFICATION OF MATERIALS DATA

Here we describe the classification of High Entropy Alloys (HEAs) using the d_p^c metric. In this setting the goal is to classify persistence diagrams of point clouds composed of atom positions in Atomic Probe Tomography (APT) experiments. In the numerical experiments

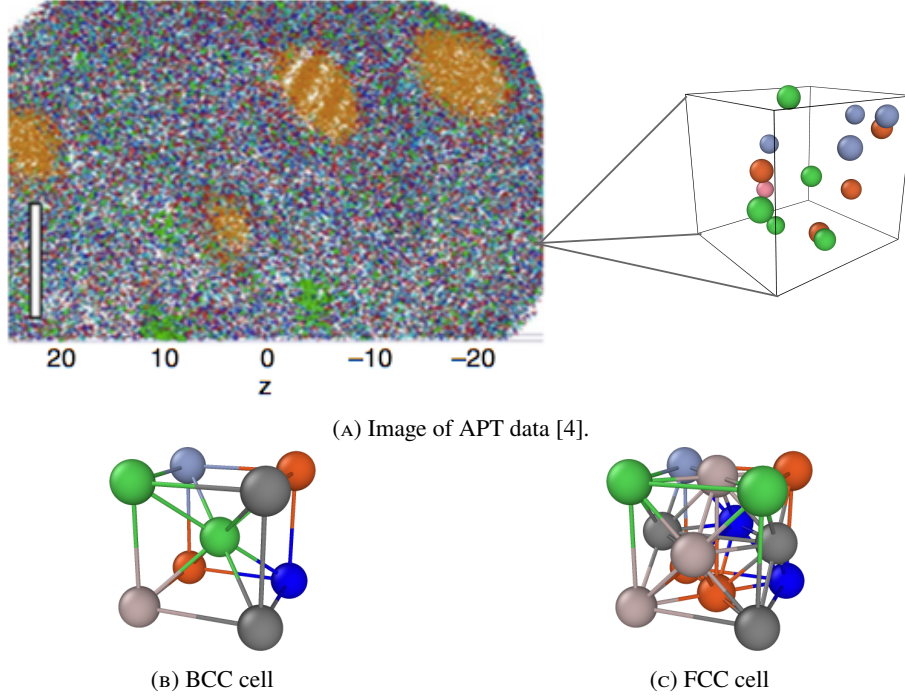
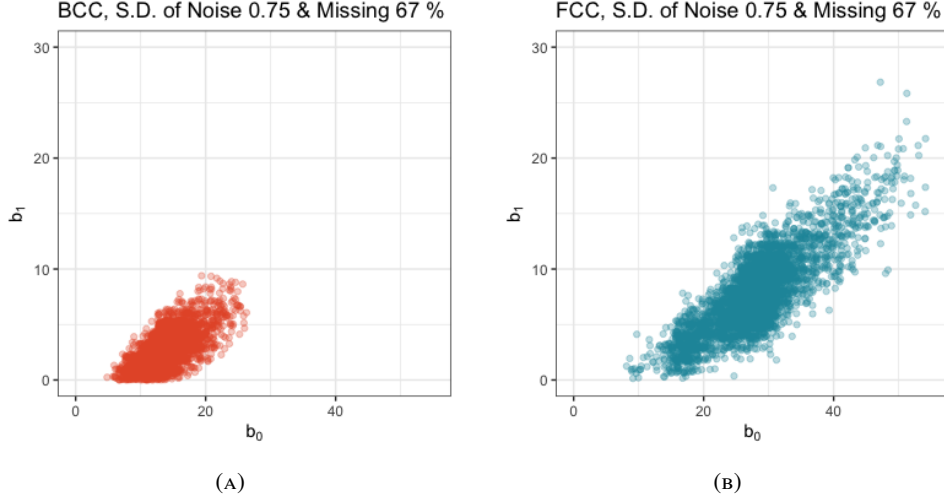


FIGURE 4. Each pixel in (A) represents a different atom. We consider neighborhoods around each atom for the local crystal structure. One may observe certain patterns in this image, e.g. the orange regions are copper rich. These copper-rich regions have a different crystal structure as compared with the rest of the dataset. And to the eye, no pattern appears to exist in the other region. Indeed, putting a single atomic neighborhood under a microscope, as shown on the right-hand side of (A), we cannot see the true crystal structure of the material, which could be either BCC (B) or FCC (C). This distinction is obscured due to the experimental noise on the data. Notice there is an essential geometric difference between the FCC and BCC structures. The scale bar in the lower left hand corner in (A) is 10 nm.

presented, the point clouds are created from synthetic data designed to accurately mimic noisy and sparse APT data and contain both BCC and FCC cells.

We classify the crystal structure of High Entropy Alloys by considering the expectation and variance of distances, as measured by the d_p^c metric, between persistence diagrams. Tools from TDA are a natural fit for this application, since the problem is inherently geometric in nature (see Fig. 4), and TDA is able to extract salient geometric information from noisy data. Moreover, the d_p^c metric is the obvious choice of metric, since it explicitly takes into account differences in cardinality.

Observe in Fig. 5 the plot of the cardinalities \mathbf{b}_0 against \mathbf{b}_1 . This plot shows the difference in 1-dim features between the two classes. FCC structures have larger point clouds, and consequently, a greater number of 0-dim features. Observe in Fig. 6 that the number of 0 and 1-dim features are greater in the FCC diagram than the BCC diagram. These differences

FIGURE 5. Plot of \mathbf{b}_0 against \mathbf{b}_1 for BCC (A) and FCC (B).

are consistent across the different noise levels and percentages of missing points tested here. This idea agrees with our materials intuition, since a BCC unit cell has fewer atoms than an FCC unit cell.

Counting (see Figs. 4B to 4C) one may see that a BCC unit cell has 2 atoms, one at the center and $1/8^{th}$ of an atom at the unit cell's corners. Similarly, an FCC unit cell has 4 atoms; the same $1/8^{th}$ of the corner atoms plus $1/2$ of each of the 6 atoms on the cell's faces. In both cases, the atoms on the faces and lattice points are shared with neighbors and are only counted as a proportion contributing to the unit cell. Thus cardinality differences may play a large role in the classification features, and to that end, we consider the d_p^c metric.

Write X_q as the persistence diagram generated by atom positions $q = (q_1, \dots, q_M)^T$. For the classification problem, we are interested in modeling $\pi_j = \mathbb{P}(Y_i = j \mid X)$, the probability of persistence diagram Y_i being in class j , for $j = 0$ (BCC) or $j = 1$ (FCC) and where X is a collection of persistence diagrams. To that end, the logistic regression model considered is

$$(5) \quad \log \left(\frac{\pi_j}{1 - \pi_K} \right) = \alpha + \sum_{\ell=1}^P \varphi_{\ell}(\Sigma_{\ell}) + \xi$$

where φ_{ℓ} is some pertinent smooth function, Σ_{ℓ} is the ℓ^{th} row of the feature matrix $\Sigma \in \mathbb{R}^{2N \times 4}$, and ξ is mean-zero normally distributed noise.

To classify these crystal structures, a feature matrix $\Sigma \in \mathbb{R}^{2N \times 4}$ is created. Here N is the number of diagrams in the training set, which is composed of both BCC and FCC persistence diagrams. An arbitrary row of the feature matrix in Eq. (5) is $\Sigma_i = (\mathbb{E}_{ij}^0, \mathbb{E}_{ij}^1, \text{Var}_{ij}^0, \text{Var}_{ij}^1)$, which is the explanatory variable Σ_j in our model Eq. (5). Here we write $\mathbb{E}_{ij}^k = \mathbb{E}[d_p^c(X_i^k, X_j^k)]$, $1 \leq j \leq N$, for persistence diagrams X_i, X_j of k -dimension $k = 0, 1$. Similarly, $\text{Var}_{ij}^k = \text{Var}[d_p^c(X_i^k, X_j^k)]$, $1 \leq j \leq N$, for persistence diagrams X_i, X_j with dimension 0 or 1. For the classification scheme itself, we use decision trees [24] with a 90/10% training/test split.

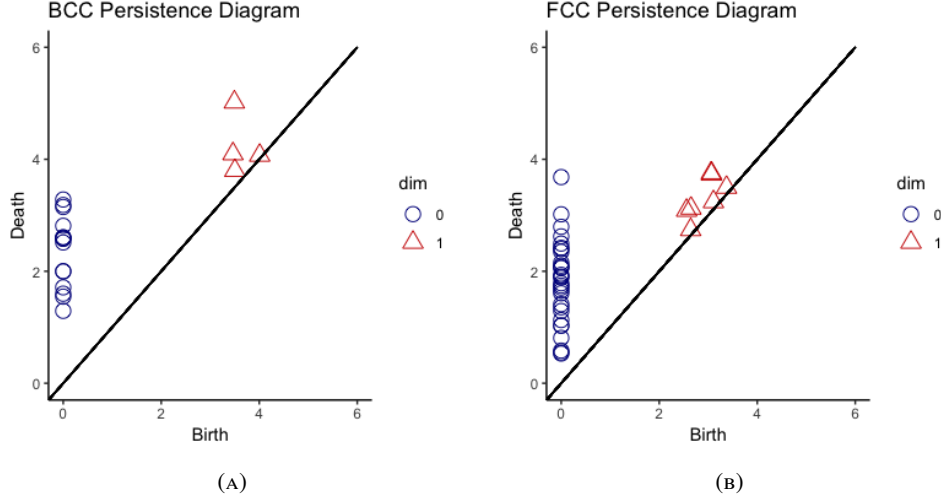


FIGURE 6. An example of persistence diagrams from BCC, (A), and FCC, (B). The data has a noise standard deviation of 0.75 and 67% missing. Note that the BCC diagram has a prominent (away from the diagonal) 1-dim feature and less 0 and 1-dim features than the FCC diagram.

The training set is comprised of persistence diagrams generated from both BCC and FCC crystal structures. The atoms in these structures are interpreted as point clouds and generate corresponding persistence diagrams, see Fig. 6. In the numerical experiments, 4 different levels of noise are considered to model the true APT datasets better. The studies [3, 4] estimate that up to 67% of the data is missing. However, an estimate for the standard deviation of the experimental noise is not provided. The classification scheme was run iteratively through the different levels of additive noise to understand more clearly the impact these defects had on the classification.

For the training step, we compute the d_p^c distance between all diagrams in the training set in turn, for dim 0, 1. This yields d_p^c distances for BCC vs. BCC, BCC vs. FCC, and FCC vs. FCC diagrams, from which one computes the first and second moments. These statistical moments are the features used in the classification for the model in Eq. (5). Having the first and second moments in hand, the tree-based classifier is trained on these features.

Then for any unknown crystal structure in the test set, its persistence diagram and d_p^c distances from the test instance to those persistence diagrams in the training set are computed and again first and second moments are calculated. The feature vector of the unknown crystal structure is then input into the decision tree. The tree finds the best fit for the features from an additive model Eq. (5) and returns the class probabilities for the unknown structure.

Fig. 8 demonstrates the presence of heteroscedasticity between \mathbf{b}_0 and \mathbf{b}_1 . Indeed, there is an increase in variance as \mathbf{b}_0 increases and then a tapering off of the number of points with larger neighborhoods. Following Proposition 3.5, the regression of \mathbf{b}_1 against the square of \mathbf{b}_0 is computed as in Eq. (4); the Breusch-Pagan test confirms the heteroscedasticity of the model with a p -value of 9.3×10^{-54} for FCC cells and a p -value of 2.01×10^{-47} for BCC cells.

τ	c -value	Accuracy
0.0	0.01	99%
0.25	0.05	98.4%
0.75	0.03	96.5%
1.0	0.13	96.4%

TABLE 1. Accuracy, as percent correct, with 10 fold cross-validated grid search for an optimal c -value in the different cases considered. In each case, we considered 67% data missing and added $\mathcal{N}(0, \tau^2)$ noise to the data.

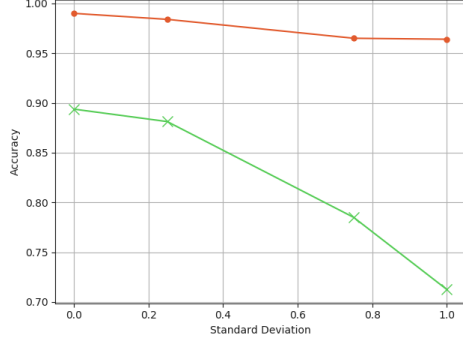


FIGURE 7. 10-fold Cross Validation Score for d_p^c and Wasserstein distances, plotted against the standard deviation of the noise. In each instance, the data had 67% missing.

Fig. 8 provides 95% prediction intervals for \mathbf{b}_1 based on the weighted least squared regression analysis of Proposition 3.5. Indeed, it yields the upper bound for a typical FCC atomic neighborhood considered here with cardinality 30, given by

$$d_p^c(X^1, Y^1) \leq \left(\frac{1}{30} \min_{\pi \in \Pi_m} \sum_{i=1}^n \min(c, \|x_i^1 - y_{\pi(i)}^1\|_{\infty})^p + 0.2749 * c^p \right)^{\frac{1}{p}}.$$

In addition, since we choose $c < 1$, the bound is essentially the optimal mapping, not necessarily a bijection, between X^1 and Y^1 . Furthermore, note that c not only penalizes differences in cardinality but also allows one to see small geometric differences between point clouds. A large c obscures finer geometric differences. Hence, there is a trade-off between penalizing cardinality and looking at subtle geometric differences.

Based on previous analysis, when computing the d_p^c distances, we use $p = 2$ to mimic traditional Euclidean distance and find different values of c via grid search for different levels of noise considered. In each case, we look at 10 values of c , geometrically spaced between 0.01 and 1. The results are presented in Table 1.

The identified topological features successfully classify BCC and FCC diagrams at better than 96% accuracy. The dataset includes 500 crystal structures, evenly split between BCC and FCC cells. Numerical experiments use training/testing splits of 90/10%. The accuracy results are presented in Table 2. In each case considered here, smaller c -values give better accuracy results than values closer to 1.

To verify the classification, 10-fold cross validation of the model is implemented. These results are shown in Table 2, for the setting with $\mathcal{N}(0, 0.75^2)$ additive noise and 67% missing. As a comparison, the same methodology is used but with the Wasserstein distance. In the numerical results presented here, the persistence diagrams were constructed using the C++ Ripser software, and scikit-learn was implemented for decision trees.

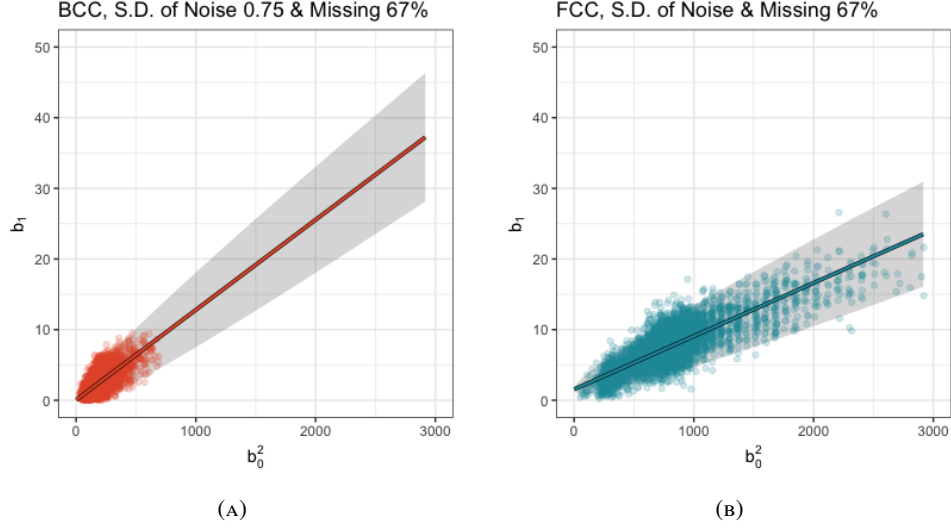


FIGURE 8. Plots of cardinalities for the materials data with $\mathcal{N}(0, 0.75^2)$ noise and 67% missing, along with the weighted least squares fit line and 95% prediction intervals. A small amount of noise is added so that the discrete-valued points have less overlap.

<i>Distance metric classification</i>	<i>Accuracy</i>
10-fold Accuracy, d_p^c	96.4%
10-fold Accuracy, Wasserstein	71.25%

TABLE 2. Accuracy scores with 90/10% train-test split with 67% missing data and $\mathcal{N}(0, 0.75^2)$ added noise.

5. CONCLUSIONS

This work combines statistical learning and topology, classifying the crystal structure of a noisy and sparse APT dataset as either BCC or FCC. Previously, APT experiments were used to see what type of atoms are present in a local neighborhood [3]. Viewed through the lens of computational topology, these local neighborhoods can be seen as point clouds and are a rich source of geometric information. By extracting the persistent homology of these point clouds, we were able to classify the crystal structures based on features derived from the new metric on persistence diagrams, denoted herein by d_p^c . This distance is unique when compared with existing distances on persistence diagrams in that it explicitly penalized differences in cardinality between the persistence diagrams being compared.

We proved a stability result for the d_p^c metric, demonstrating that small perturbations of the underlying point clouds resulted in small changes to the d_p^c distance. We also provided guidance for the choice of the c parameter by looking at confidence bounds using a function of the cardinalities of the persistence diagrams. These bounds can be used as guidance as to the range of values the parameter c in the d_p^c distance can take for a specific dataset.

The classification results presented herein could aid materials science researchers to provide a previously unavailable representation of the local atomic environment. Indeed,

as APT experiments produce datasets on the order of 10 million atoms, materials science research has moved into the realm of big data, and the necessary computational and modelling tools have yet to be developed for this regime [25]. Our method, coupled with our ongoing research [26] into the local atomic structure of high entropy alloys, aims to help close that gap.

ACKNOWLEDGMENTS

The authors would like to thank Professor David Keffer from the University of Tennessee’s College of Engineering, Materials Science department for the code to create realistic APT datasets and for useful discussions about the datasets and Professor Kody J.H. Law of the University of Manchester’s School of Mathematics for insightful discussions.

REFERENCES

- [1] A. Ziletti, D. Kumar, M. Scheffler, L. M. Ghiringhelli, Insightful classification of crystal structures using deep learning, *Nature communications* 9 (1) (2018) 2775.
- [2] N. W. McNutt, O. Rios, V. Maroulas, D. J. Keffer, Interfacial li-ion localization in hierarchical carbon anodes, *Carbon* 111 (2017) 828–834.
- [3] M. K. Miller, T. F. Kelly, K. Rajan, S. P. Ringer, The future of atom probe tomography, *Materials Today* 15 (4) (2012) 158–165.
- [4] L. J. Santodonato, Y. Zhang, M. Feygenson, C. M. Parish, M. C. Gao, R. J. Weber, J. C. Neuefeind, Z. Tang, P. K. Liaw, Deviation from high-entropy configurations in the atomic distributions of a multi-principal-element alloy, *Nature communications* 6 (2015) 5964.
- [5] P. Bettini, R. Specogna, Computation of stationary 3d halo currents in fusion devices with accuracy control, *Journal of Computational Physics* 273 (2014) 100–117.
- [6] H. Edelsbrunner, D. Letscher, A. Zomorodian, Topological persistence and simplification, in: *Foundations of Computer Science, 2000. Proceedings. 41st Annual Symposium on*, IEEE, 2000, pp. 454–463.
- [7] A. Zomorodian, G. Carlsson, Computing persistent homology, *Discrete & Computational Geometry* 33 (2) (2005) 249–274.
- [8] G. Carlsson, A. Zomorodian, A. Collins, L. J. Guibas, Persistence barcodes for shapes, *International Journal of Shape Modeling* 11 (02) (2005) 149–187.
- [9] L. Wasserman, Topological data analysis, *Annual Review of Statistics and Its Application* 5 (2018) 501–532.
- [10] B. Wang, G.-W. Wei, Object-oriented persistent homology, *Journal of computational physics* 305 (2016) 276–299.
- [11] A. Marchese, V. Maroulas, Topological learning for acoustic signal identification, in: *Information Fusion (FUSION), 2016 19th International Conference on*, IEEE, 2016, pp. 1377–1381.
- [12] A. Marchese, V. Maroulas, J. Mike, K-means clustering on the space of persistence diagrams, in: *Wavelets and Sparsity XVII*, Vol. 10394, International Society for Optics and Photonics, 2017, p. 103940W.
- [13] J. L. Mike, V. Maroulas, Nonparametric estimation of probability density functions of random persistence diagrams (March 2018). [arXiv:1803.02739](https://arxiv.org/abs/1803.02739).
- [14] H. Adams, T. Emerson, M. Kirby, R. Neville, C. Peterson, P. Shipman, S. Chepushtanova, E. Hanson, F. Motta, L. Ziegelmeier, Persistence images: A stable vector representation of persistent homology, *The Journal of Machine Learning Research* 18 (1) (2017) 218–252.
- [15] D. Cohen-Steiner, H. Edelsbrunner, J. Harer, Stability of persistence diagrams, *Discrete & Computational Geometry* 37 (1) (2007) 103–120.
- [16] A. Marchese, V. Maroulas, Signal classification with a point process distance on the space of persistence diagrams, *Advances in Data Analysis and Classification* 12 (3) (2018) 657–682.
- [17] F. Chazal, V. de Silva, S. Oudot, Persistence stability for geometric complexes, *Geometriae Dedicata* 173 (1) (2014) 193–214.
- [18] H. Edelsbrunner, J. Harer, *Computational Topology: An Introduction*, American Mathematical Society, Providence, RI, 2010.
- [19] B. T. Fasy, F. Lecci, A. Rinaldo, L. Wasserman, S. Balakrishnan, A. Singh, et al., Confidence sets for persistence diagrams, *The Annals of Statistics* 42 (6) (2014) 2301–2339.
- [20] F. Chazal, D. Cohen-Steiner, Q. Mérigot, Geometric inference for probability measures, *Foundations of Computational Mathematics* 11 (6) (2011) 733–751.

- [21] M. Kerber, D. Morozov, A. Nigmatov, Geometry helps to compare persistence diagrams, *Journal of Experimental Algorithmics (JEA)* 22 (2017) 1–4.
- [22] D. Schuhmacher, B.-T. Vo, B.-N. Vo, A consistent metric for performance evaluation of multi-object filters, *IEEE Transactions on Signal Processing* 56 (8) (2008) 3447–3457.
- [23] B. Efron, T. Hastie, *Computer age statistical inference*, Vol. 5, Cambridge University Press, 2016.
- [24] J. Friedman, T. Hastie, R. Tibshirani, *The elements of statistical learning*, Springer series in statistics New York, NY, USA., 2009.
- [25] M. A. Katsoulakis, N. Zabaras, Special issue: Predictive multiscale materials modeling, *Journal of Computational Physics* 338 (1).
- [26] A. Spannaus, V. Maroulas, D. Keffer, K. J. H. Law, Bayesian point set registration, in: *2017 Matrix Annals*, Springer, 2017.

DEPARTMENT OF MATHEMATICS - UNIVERSITY OF TENNESSEE, KNOXVILLE, TN 37996
E-mail address, Corresponding author: vmaroula@utk.edu

DEPARTMENT OF MATHEMATICS - UNIVERSITY OF TENNESSEE, KNOXVILLE, TN 37996
E-mail address: cputman@vols.utk.edu

DEPARTMENT OF MATHEMATICS - UNIVERSITY OF TENNESSEE, KNOXVILLE, TN 37996
E-mail address: aspannaus@utk.edu